IEEE Open Journal of
Circuits and Systems

Received 3 June 2024; revised 12 July 2024 and 1 September 2024; accepted 25 September 2024. Date of current version 13 December 2024.

Digital Object Identifier 10.1109/OJCAS.2024.3472124

ASIC Current-Reuse Amplifier With MEMS Delta-E Magnetic Field Sensors

PATRICK WIEGAND [1], SEBASTIAN SIMMICH [1] (Graduate Student Member, IEEE), FATIH ILGAZ [2], FRANZ FAUPEL [2], BENJAMIN SPETZLER [3] (Member, IEEE), AND ROBERT RIEGER [1] (Senior Member, IEEE)

[1] Chair for Networked Electronic Systems, Department of Electrical and Information Engineering, Faculty of Engineering, Kiel University, 24143 Kiel, Germany
[2] Chair for Multicomponent Materials, Department of Materials Science, Faculty of Engineering, Kiel University, 24143 Kiel, Germany
[3] Micro- and Nanoelectronic Systems, Department of Electrical Engineering and Information Technology, Ilmenau University of Technology, 98693 Ilmenau, Germany

This article was recommended by Associate Editor S. Shah.

Corresponding author: P. WIEGAND (e-mail: pw@tf.uni-kiel.de)

This work was supported by the German Research Foundation (Deutsche Forschungsgemeinschaft, DFG) through the project A4 of the Collaborative Research Center CRC 1261 Magnetoelectric Sensors: From Composite Materials to Biomagnetic Diagnostics.

ABSTRACT An application specific integrated circuit (ASIC) and a custom-made microelectromechanical system (MEMS) sensor are presented, designed to function together as a sensor system for measuring low amplitude low frequency magnetic fields. The MEMS system comprises several free-standing double-wing magnetoelectric resonators with a size of 900 μm x 150 μm to measure alternating magnetic fields in the sub-kilohertz regime. It utilizes piezolelectric (AlN) and magnetostrictive (FeCoSiB) layers to exploit the delta-E effect for magnetic field sensing. On the ASIC a three-channel current-reuse amplifier with lateral bipolar transistors in the input stage is implemented occupying a chip area of 0.0864 mm^2. Measurements demonstrate a voltage gain of 40 dB with a 3-dB bandwidth of 75 kHz and an input referred noise floor of 8 nV/$\sqrt{}$Hz while consuming 199 μW per channel. The sensor system is capable of detecting magnetic fields with a limit of detection (LOD) of 16 nT/$\sqrt{}$Hz for single sensor elements. By operating three sensor elements in parallel, one on each amplifier channel, the LOD is further reduced to 10 nT/$\sqrt{}$Hz. Owing to the high reproducibility of the sensor elements, this improvement in the LOD is close to the ideal value of $\sqrt{3}$. The results imply that the system can be scaled to large numbers of sensor elements without principle obstacles.

INDEX TERMS Multichannel amplifier, CMOS, NEF, MEMS resonator, magnetic field sensor, magnetoelectric sensor, delta-E effect, biomedical.

I. INTRODUCTION

INTEGRATED magnetic field sensors are a growing field of investigation in numerous research areas. Detecting magnetic signals with high spatial resolution or very low LOD is relevant in a variety of fields and applications including the automotive industry [1], object localization [2], healthcare [3], [4], [5], information technology [6], or space applications [7]. MEMS with thin film magnetoelectric sensors have attracted interest in recent years [8], [9], [10] and macroscopic sensors have shown to be capable of detecting magnetic fields in the picotesla range and withstand a broad temperature range [11], [12], [13], [14]. The sensors employ a combination of mechanically coupled magnetostrictive and piezoelectric layers to exploit the direct magnetoelectric effect but are limited to small bandwidths of a few Hz around the resonance mode used [15], [16], [17]. This bandwidth limitation can be overcome by utilizing the delta-E effect [18] of the magnetostrictive layer. This layer induces additional magnetostrictive strain in the resonator, changing its stiffness in the presence of a magnetic field [19], [20], [21]. This detunes the resonator, i.e., the resonance frequency of the sensor shifts.

To measure magnetic fields, the resonator is electrically excited at its nominal resonance frequency by a voltage source and a read-out circuit determines the sensor impedance at that specific frequency. A resonance frequency shift alters the impedance at the excitation frequency, which is electrically measurable. With this approach the magnetic field is not detected directly, but rather measured as a modulation of the electric excitation power. The signal thus obtained, is amplified and eventually digitized. Finally, the signal is demodulated in the digital domain to extract the information about the magnetic field. Based on the delta-E effect sensor concept, magnetic field sensors have been presented with free-standing cantilever geometries [14], [22], [23], nanoplate resonators [24], [25] and surface acoustic wave devices [26], [27], [28] typically operated with external, discrete electronics.

In this work, microscopic MEMS resonators and an ASIC amplifier are presented. With this setup, resonator arrays can be formed, parallelizing resonators to enhance the LOD of the sensors system.

When operating the sensors in delta-E mode, the readout electronics have to meet high demands, especially regarding noise and bandwidth. Bipolar junction transistors (BJT) can provide very low noise when used in the input stage of an amplifier [29], [30]. Moreover, the finite small-signal base input resistance of the BJT is employed here to form a voltage divider with the sensor element for reading out the modulated excitation voltage as explained in Section II. The BJTs can be manufactured as lateral devices in a conventional CMOS process technology and so provide a good compromise between performance and manufacturing costs [31]. Therefore, despite their reduced performance, especially in terms of the typical forward current gain β compared to vertical devices that require a costlier BiCMOS technology, lateral BJTs (L-BJT) are used in the circuit presented here.

To increase the capability of measuring small amplitude magnetic fields, the microscopic size of the MEMS and ASIC chips can be exploited by grouping sensors in arrays. As shown in [32], the use of n sensors placed in a homogeneous magnetic field increases the measured signal amplitude by a factor of n. Conversely, the noise of the sensors only increases by $\sqrt{n}$, as it is generated by uncorrelated noise processes in the sensor system. Thus, the signal to noise ratio (SNR) and the LOD improve by a factor of $\sqrt{n}$.

In Section II we present additional detail of the ASIC amplifier design (for which we presented preliminary results in [33]) and we report its operation in direct combination with custom-made MEMS resonator sensors. New measured results are presented in Section III which confirm the low LOD of the combined ASIC-MEMS system. It is followed by a discussion in Section IV and conclusions in Section V.

II. SENSOR SYSTEM DESIGN

The MEMS sensor elements and the ASIC amplifier are specifically designed to work in array configurations. Therefore, a low-power multichannel amplifier is implemented which occupies only a small chip area and can be operated in an open-loop configuration. The sensor elements

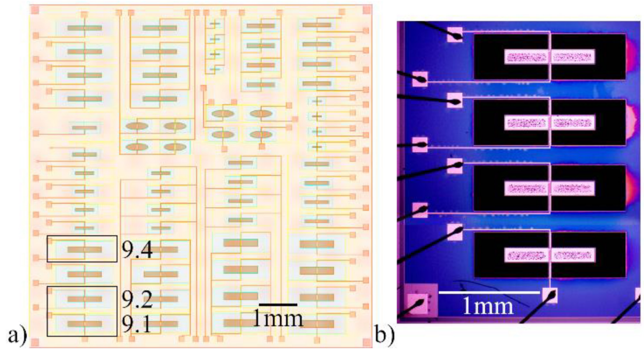

FIGURE 1. a) The MEMS layout measures 9 mm x 9mm. It offers space for 66 resonators ranging from 256 μm x 40 μm to 900 μm x 200 μm in size. The resonators used in this work are marked in black. b) Top view photograph of the resonators 9.1 to 9.4 with a size of 900 μm x 150 μm - Visible are the aluminum top electrodes and the wires connecting the electrodes to the bonding pads.

can be fabricated in a large number and with a high reproducibility of the device characteristics [34]. In Fig. 1a the layout of the fabricated MEMS chip is shown, where test structures with 66 sensor elements were fitted in an area of 9 mm x 9 mm. Fig. 1b is a microphotograph of a selected array of four nominally identical sensor elements, of which the three best matching ones (9.1, 9.2, 9.4) are chosen for the array setup reported here.

The MEMS resonators offer resonance modes in the range of 10 kHz up to 1 MHz, reaching into a frequency range where high gain is challenging to achieve in the target CMOS technology without considerable increase in power consumption. The available L-BJT transistors yield a transit frequency of about 30 MHz, which is the technological limit above which the single transistor yields no more usable voltage gain. Here, it is proposed to operate the amplifier in an open-loop configuration despite its potentially higher sensitivity towards process and temperature variations. This way higher gain is maintained around the 3dB-cut-off frequency and also the additional load of a closed-loop feedback network is avoided.

A diagram of the measurement setup with the sensor in delta-E mode is shown in Section III and will be explained in more detail there. Basically, the magnetic field measurement works as follows: The magnetic signal of interest induces an impedance change in the sensor element which is determined by observing the voltage between the piezo electrodes. The amplifier is connected to the sensor via blocking capacitors. Around the resonance frequency of about 350 kHz these blocking capacitances pose negligible impedance, and the small-signal resistance of the amplifier input is dominated by r_i, the base-emitter resistance of the L-BJT. Resistance r_i together with sensor impedance Z_S form a voltage divider with attenuation A_S, so that

$$\frac{v_{be}}{v_{ex}} = A_S = \frac{r_i}{r_i + Z_S} \approx \frac{\beta}{\beta + Z_S g_m} \tag{1}$$

where g_m is the L-BJT transconductance, approximately given by I_C/V_T, and V_T is the thermal voltage. The

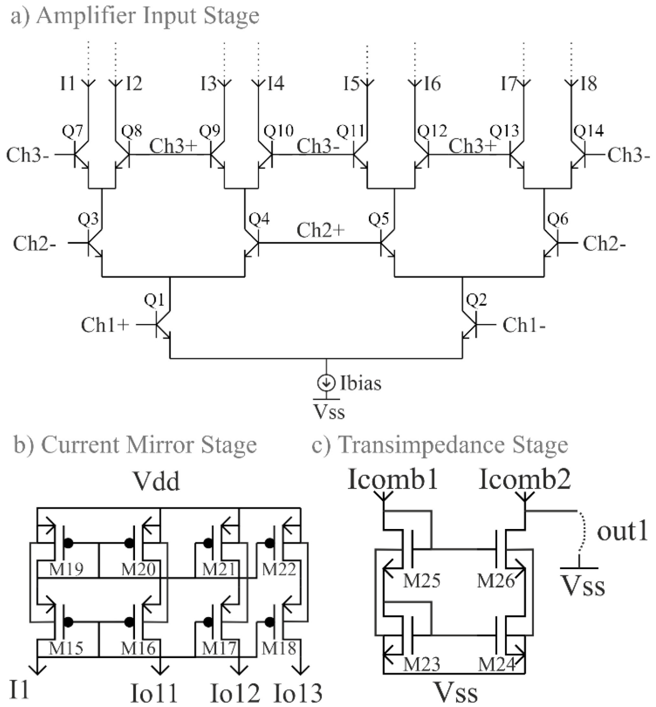

FIGURE 2. Schematic of the three main stages of the three-channel current-reuse amplifier. a) The analog input stage utilizes L-BJTs and offers three stacked channels. b) The current mirror stage mirrors every current from the input stage thrice and recombines them to retrieve the individual inputs. c) The transimpedance stage transforms the currents provided by the current mirror stage to a voltage. Source: [33].

approximation holds for small base spreading resistance and negligible base-emitter capacitance [35]. The sensitivity of the readout circuit to changes in Z_S is determined by this divider, yielding

$$\left|\frac{dA_S/dZ_S}{A_S}\right| = \frac{g_m}{\beta + Z_S g_m} \tag{2}$$

Using typical values for g_m of 500 μA/V, $Z_S = 45$ kΩ and, owing to the limited efficiency L-BJT implementation a β of only 20, yields $A_S = 0.5$ and a sensitivity of $(85\ \text{k}\Omega)^{-1}$.

A. ASIC AMPLIFIER DESIGN

The ASIC is designed and fabricated in a 350 nm CMOS process technology. This mature technology was chosen for its attractive price-to-performance ratio and its well characterized analogue device models.

The amplifier employs the current-reuse configuration to achieve a favorable noise-to-power trade-off [36]. The differential input stage shown in Fig. 2a offers three channels. It employs L-BJTs as input transistors. Starting with two transistors (Q1 and Q2) for the first channel, every following channel doubles the number of transistors (Q3 ... Q6 resp. Q7 ... Q14) such that the output currents of the previous channel can be reused as tail current for the next channel differential input pairs. This lowers the power consumption per channel and thus the noise efficiency factor (NEF) of the amplifier. The NEF is defined as

$$NEF \;=\; V_{rms,in}\sqrt{\frac{2 \cdot I_{tot}}{\pi \cdot V_T \cdot 4k_B T \cdot f_c}} \tag{3}$$

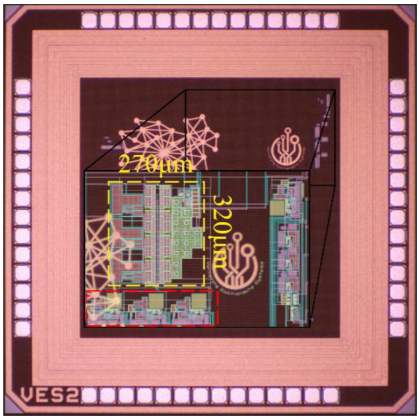

FIGURE 3. Microphotograph of the fabricated ASIC. Because a passivation layer blocks the direct view to the circuits, the layout is projected on top in the enlarged view of the inset. It shows the occupied area (270 μm x 320 μm) of the current-reuse amplifier in the yellow dashed box. The red line marks the output buffers.

where $V_{rms,in}$ is the integrated input referred noise, I_{tot} is the total current drawn by the amplifier, k_B is the Boltzmann constant, T is the temperature in kelvin, and f_c the amplifier cutoff frequency [37].

For optimum operation all input transistors have to work in saturation. Therefore, a resistive network on the ASIC generates appropriate common-mode voltages $V_{CM,n}$ for each channel individually. The input channels are supplied from a bias current I_{bias} of 50 μA. The resulting base-emitter voltage V_{BE} of the transistors is approximately 800 mV. Starting at channel 1 with at least V_{BE} above the negative voltage supply ($V_{SS} = -1.5$ V), the common-mode voltages are staggered by an overdrive voltage of $V_{OV} = 250$ mV for each following channel to ensure the transistors are operated in saturation.

Every output current I_1–I_8 emanating from the input stage is a weighted sum of all channel contributions. To retrieve the differential analogue signals of the individual input channels these currents have to be recombined properly [38]. As an example, the addition of I_1–I_4 yields the current provided by the positive input of channel 1 as contributions from channel 2 and 3 cancel out. With six different input signals (three symmetrical channels) six additions are necessary. Every recombination is the sum of four currents, leading to three copies of every current I_1-I_8 as shown in Fig. 2b and 24 current mirrors in total. In a final step, these recombined currents are converted to a single-ended voltage output in a transimpedance stage as shown in Fig 2c.

Fig. 3 shows a microphotograph of the fabricated ASIC amplifier. Because a passivation layer blocks the view of the implemented circuits, the layout is superimposed in the enlarged area. The amplifier occupies an area of approximately 270 μm x 320 μm. Three buffer amplifiers are placed below, to drive the output signal for external loads. They will not be necessary in a final system, where on-chip demodulation and analog-to-digital conversion is targeted.

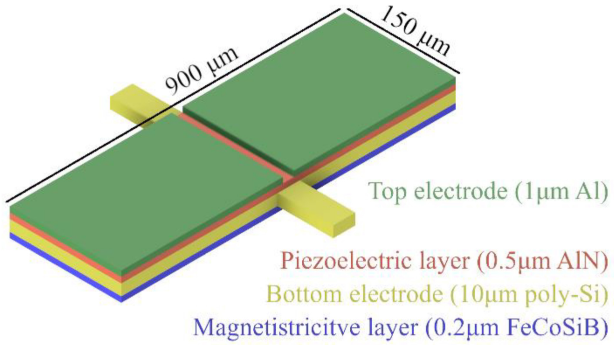

FIGURE 4. Layer stack of the MEMS resonator sensors with a length of 900 μm and a width of 150 μm. The thickness of each layer is given in parentheses.

B. MEMS DESIGN

MEMS consisting of multiple thin film layers are used as a base for the sensor elements. Free-standing double wing resonators are etched from a SOI wafer. A piezoelectric layer is utilized to excite the sensor in resonance and read it out simultaneously. The sensing element of the resonator is a magnetostrictive single layer made of $(Fe_{90}Co_{10})_{78}Si_{12}B_{10}$ (FeCoSiB). Except from the magnetostrictive FeCoSiB layer, the MEMS chips are manufactured in a commercially available production process. The MEMS resonator layer stack is shown in Fig. 4. It consists of a 10-μm-thick doped poly-Si substrate, which also operates as a backside electrode, 0.2-μm-thick pad oxide to isolate the back electrode from following layers where needed, 0.5-μm-thick piezoelectric AlN to excite the sensor and retrieve its impedance and 1-μm-thick Aluminum as a top electrode. Afterwards, we deposited a 0.2-μm-thick FeCoSiB layer on the rear side in a shadow mask process. No further postprocessing was done to the sensor elements. More details are reported in [34]. The resonators used in this work measure 900 μm in length and 150 μm in width with an anchoring in the middle of the long axis as shown in Fig. 4.

III. MEASUREMENTS

A. MEASUREMENT SETUP

The amplifier measurements are conducted using a lock-in amplifier (MFLI, Zurich instruments, Switzerland) to measure gain, phase and noise while the ASIC is placed in an electrically shielded chamber (dbSAFE DUO, DVTEST INC., Canada). The used lock-in amplifier is well suited for noise measurements as it offers a low input noise of only 2.5 nV/$\sqrt{}$Hz. A laboratory power supply (EDU36311A, Keysight Technologies, Inc., USA) is used to generate the supply voltage for the ASIC with $V_{dd} = +1.5$ V, $V_{ss} = -1.5$ V and ground (GND) $V_{GND} = 0$ V. For noise measurements, the power supply was replaced by a pair of 1.5 V batteries.

For magnetic measurements, MEMS and ASIC are placed inside the electrically shielded chamber for testing. Additionally, the MEMS sensors are magnetically shielded (Zero Gauss Chamber, Aaronia AG, Germany). This shielding setup was established in [39]. Inside this shielding chamber two separate coils provide homogenous magnetic fields along the long axis of the resonators One coil provides alternating and the other one DC magnetic fields. The coil for the alternating field generates a synthetic sinusoidal signal to be measured, while the DC field provides the B_{DC} working point field for optimal operation of the resonators. The resonators are placed in the middle of these coils. A schematic of this setup is shown in Fig. 5.

A current source (6221, Keithley Instruments, Inc., USA) operates the AC coil with a sine wave providing a magnetic field of $B_{AC} = 500$ nT at $f_{AC} = 10$ Hz as a magnetic signal to be measured. These parameters are chosen, as 10 Hz is a typical frequency in the envisioned application in healthcare, whereas 500 nT is chosen to yield clearly readable peaks in the amplitude spectrum. A DC current source (BOP 20-10ML, Kepco, INC., USA) is connected with the DC coil to generate a field of $B_{DC} = 0.5$ mT to bias the resonators in their operating point. To electrically excite the resonators at their resonance frequency $f_r = 343.6$ kHz with $v_{ex} = 100$ mV a lock-in amplifier (HF2LI, Zurich instruments, Switzerland) is used as an oscillator. This voltage amplitude is chosen as it yields high MEMS sensitivity and makes good use of the amplifiers output range. The rear side electrode of the MEMS chip is connected to this oscillator. The top electrodes of three resonators are connected via DC blocking capacitors ($C_{1,n} = C_{2,n} = 10$ μF) to the negative input of the three channels of the ASIC current-reuse amplifier. The positive inputs of the amplifier are connected to GND, also via DC-blocking capacitors. The single-ended outputs of the amplifiers are wired to the lock-in amplifier to digitize the signal. The amplifiers are used in open-loop configuration. Since the channels are averaged in the end, small variations in gain are negligible and no feedback for closed-loop operation is necessary. In some cases, idle current supplies are switched off (e.g., no alternating magnetic signal is used when measuring impedance).

For impedance measurements, the presented amplifier is exchanged for a charge amplifier described in [40]. Then, the excitation frequency of the lock-in amplifier is swept. At resonance frequencies the impedance of the MEMS resonators changes rapidly, yielding a variation of the current flowing through the resonator. This current is converted to a voltage by the charge amplifier, acting as a transimpedance amplifier. The impedance of the sensor element Z_S can then be calculated with

$$Z_S = \frac{Z_f v_{ex}}{v_o} \tag{4}$$

where Z_f is the feedback impedance of the charge amplifier, v_{ex} is the excitation amplitude and v_o the measured voltage at the amplifier output [41].

Since the lock-in amplifier only provides two inputs, only two signals can be measured simultaneously. However, the signal is time invariant, so that measuring resonators

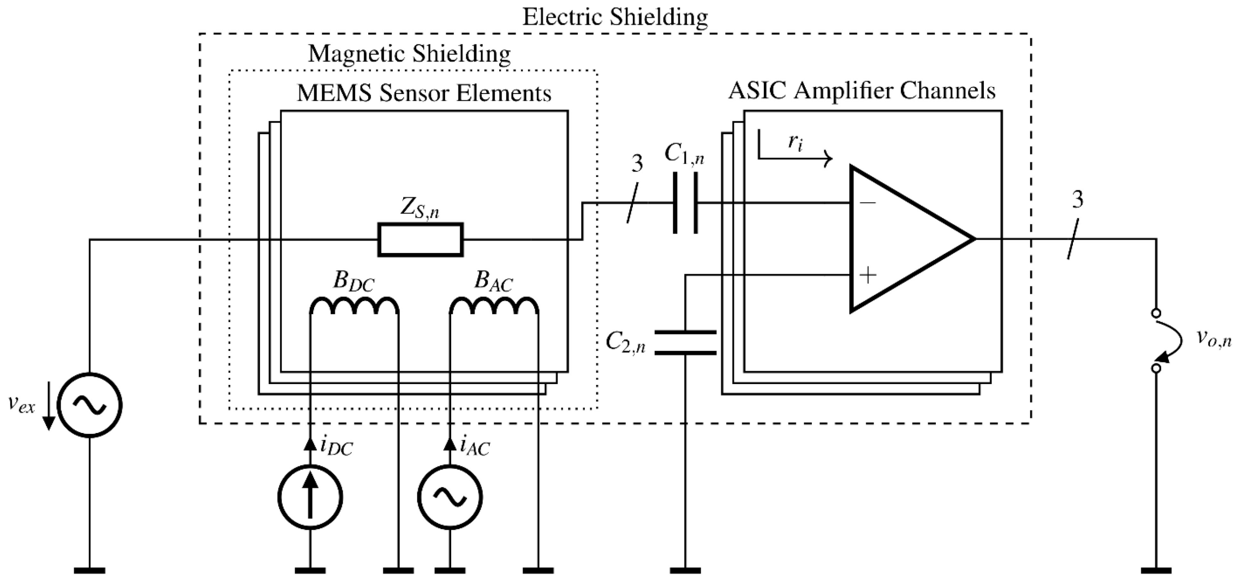

FIGURE 5. Setup to characterize the sensor system. An oscillator excites the three resonators $Z_{S,n}$ at their resonance frequency with the voltage v_{ex}. The resulting signal is amplified by the three channel current-reuse amplifier and measured at $v_{o,n}$. The coil for the bias field B_{DC} is operated by the current i_{DC} and a sinusoidal measurement signal is generated with coil B_{AC} and the current i_{AC}. The capacitances $C_{1,n}$ and $C_{2,n}$ serve as DC blocks. The MEMS resonators are magnetically and electrically shielded. The ASIC is electrically shielded.

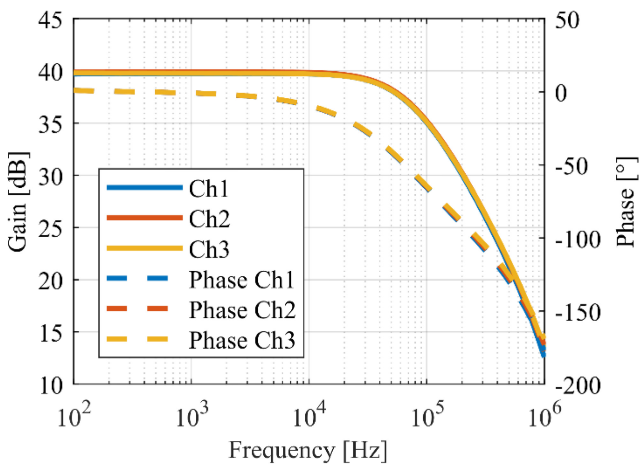

FIGURE 6. Measured gain and phase of the three-channel current-reuse amplifier with a tail current I_{bias} of 50 μA. The lines almost coincide as the channels are well matched.

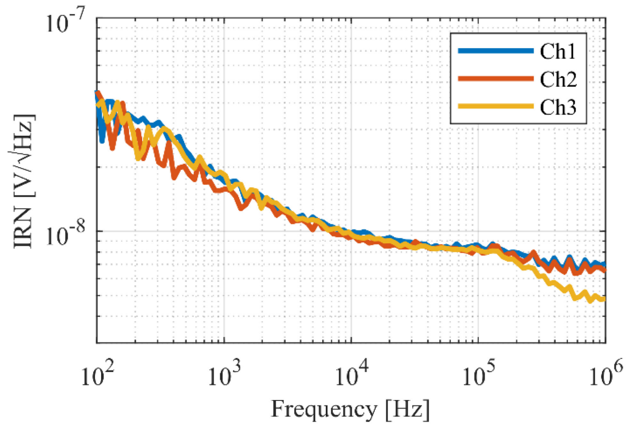

FIGURE 7. Input referred noise of the amplifier per channel with a tail current I_{bias} of 50 μA. The noise floor settles at about 8 nV/$\sqrt{}$Hz.

consecutively is not detrimental for the overall measurement results.

B. ASIC CHARACTERIZATION

The total current consumption of the amplifier measures 199 μA, when the input stage is driven with the I_{bias} current set to 50 μA. The current is distributed evenly among all channels of the amplifier, so that the current per signal channel calculates to 66 μA. The total power consumption of the amplifier is thus 597 μW, respective 199 μW per channel. The resistive network generating the DC common-mode voltages is included in this value. The DC voltages are measured as -390 mV for channel 1, -150 mV for channel 2 and 115 mV for channel 3.

The results of the open-loop gain and phase measurements are shown in Fig. 6. The 3-dB cutoff frequency of the amplifier is observed at 75 kHz. The low-frequency gain of all channels is measured as 40 dB. At the targeted resonance frequency of 343 kHz the amplifiers have a reduced gain of approximately 24 dB. Albeit the lower gain at resonance frequency, it is sufficient for the operation of the sensor system that utilizes almost the entire output range of the amplifier when exciting the resonator with $v_{ex} = 100$ mV.

For the noise measurements the channels were connected to ground potential through a capacitor. The on-chip resistive network continues to generate the common-mode voltage for the differential input channels. The measured noise floor of all three channels settles at about 8 nV/$\sqrt{}$Hz (Fig. 7) caused by noise originating from both the resistive biasing network

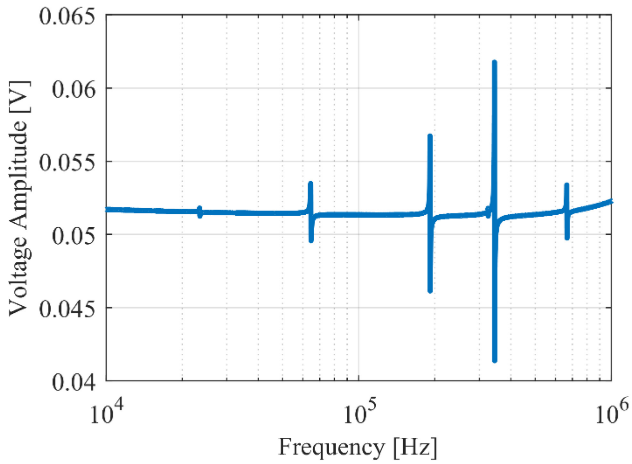

FIGURE 8. Sweep of excitation frequency plotted against voltage amplitude at the amplifiers output from 10 kHz to 1 MHz. Every peak corresponds to a resonance mode of sensor 9.1. The resonance mode with the highest amplitude located at 343kHz is used here.

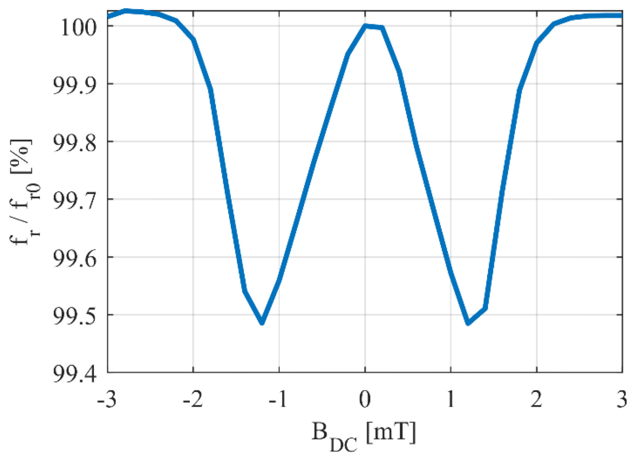

FIGURE 9. Shift of the resonance frequency f_r depending on the magnetic DC B_{DC} field applied along the long axis of the resonator 9.1 normalized to the value of $B_{DC} = 0$mT. Here the magnetic field is swept from −3 mT to 3 Mt.

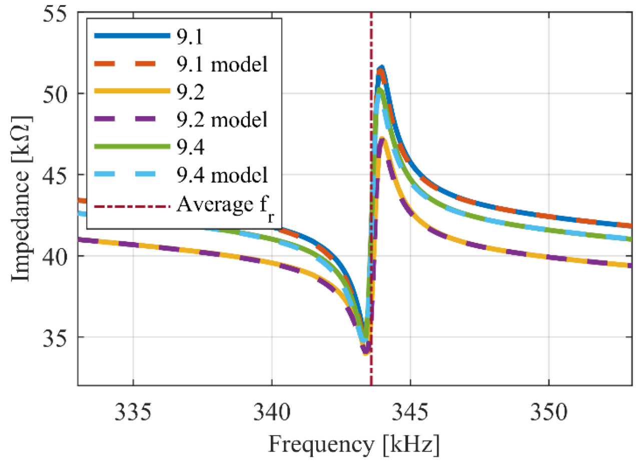

FIGURE 10. Closely matching resonance frequency curves of the three sensors at 0.5 mT DC bias field and their average resonance frequency f_r.

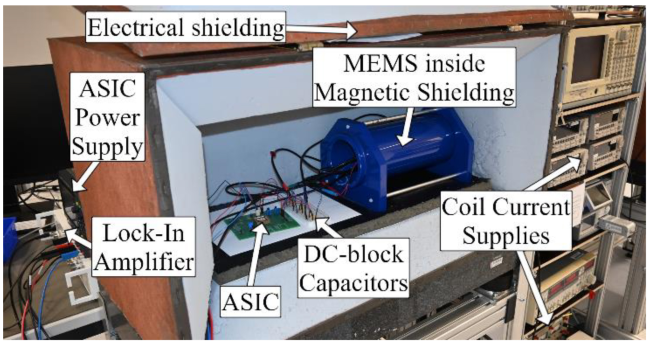

FIGURE 11. Measurement setup for the system evaluation. The setup is electrically shielded by a box covered in copper fleece. The sensor elements are additionally magnetically shielded by a cylinder made of Mu-metal. The current supplies are used to drive coils for the magnetic bias field. The coils bias the sensor elements and provide a synthetic magnetic field to be measured. The ASIC is powered by a voltage supply with ±1.5 V. The lock-in amplifier provides an oscillator output that is connected to the bottom electrode of the sensor elements and provides an AC voltage to excite the sensors in resonance. The top electrodes of the elements are connected to the ASIC amplifier via a DC-block capacitor. The amplifier output voltage is measured by the lock-in amplifier.

and the amplifier. Integrating the input referred noise (IRN) from 100 Hz to 200 kHz yields 3.92 μVrms for channel 1, 3.77 μVrms for channel 2 and 3.76 μVrms for channel 3. Using (3) leads to a NEF of about 2.7 for all channels.

C. MEMS CHARACTERIZATION

To determine the available resonance modes, a frequency sweep is conducted from 10 kHz to 1 MHz. At the resonance frequencies a sudden change in impedance is measured. As shown in Fig. 8, the sensor elements offer several resonance modes below 1 MHz. The higher the gradient at such a peak, the higher the electrical sensitivity this mode offers. We use the mode at 343 kHz in this work to exploit its high sensitivity.

Fig. 9 exemplarily shows the resonance frequency of one of the MEMS resonators as a function of the surrounding magnetic field. Here, the B_{DC} bias field is swept from −3 mT to +3 mT and for every step the resonance frequency f_r is calculated using a modified Butterworth van Dyke (mBvD) equivalent circuit model [42] fitted to the measured impedance. This measurement shows the typical w-shape expected for magnetostrictive resonators [21]. At zero DC field the resonator is rather insensitive to magnetic fields (small change of resonance frequency), whereas a large gradient (i.e., high magnetic sensitivity) is visible, e.g., at ±0.4 mT up until ±1.2 mT. At higher field strengths the effect reverses, offering another potential working point until the magnetostrictive layer reaches saturation for fields larger than ±2 mT where sensitivity decreases rapidly to zero and the sensor element reaches saturation. A working point with a large magnitude of slope is chosen, to increase the sensitivity of the resonator. Here, we use $B_{DC} = 0.5$ mT as a magnetic DC bias field since it is convenient to generate with our instruments and very similar for all three resonators in use.

To fulfil the premise of using several sensor elements in parallel to increase the overall system LOD, the sensor elements have to match closely regarding noise, sensitivity and resonance frequency. To increase the SNR, the difference of the resonance frequency across all sensor elements must satisfy the condition

$$\frac{\Delta f_r}{f_r} Q < 0.5 \tag{5}$$

where Δf_r is the difference between the resonance frequency of the single sensor element and the average resonance frequency of all used sensor elements and Q is the quality factor of the sensor elements [32]. Hence, to make use of all available channels of the current-reuse amplifier, three similar sensor elements are necessary. On the MEMS chip, four resonators with the same size of 900 μm x 150 μm are available. This resonator size is chosen as it provides a high magnetic sensitivity due to the large area that can be covered with the magnetostrictive FeCoSiB. Resonators 9.1, 9.2 and 9.4 (indicated in Fig. 1) were chosen among the four candidate devices as they exhibited the closest resonance frequency match. The resonance frequencies f_r and quality factors Q are obtained by a mBvD-fit to the impedance measurements of the sensor elements.

As shown in Fig. 10 an excellent agreement of simulations and measurements is achieved and the resonance frequencies of the three sensor elements match closely. With the DC bias field $B_{DC} = 0.5$ mT applied, the sensor elements offer resonance frequencies with a mean value of $f_r = 343.6$ kHz. Sensor element 9.1 deviates by $\Delta f_r = 5.3$ Hz, sensor element 9.2 by $\Delta f_r = 48.4$ Hz and sensor element 9.4 by $\Delta f_r = 43.5$ Hz. This results in deviations from the average resonance frequency of 0.0015% to 0.0141%, highlighting the great reproducibility of the production and post-production process. The rejected resonator 9.3 deviates by $\Delta f_r = 130$ Hz or 0.04% from the average resonance frequency. Together with Q-factors in the vicinity of 680, (5) yields values < 0.1 for the presented setup. Additionally, this impedance measurement confirms that the sensor element impedance is in the range of 45 kΩ as expected in Section II.

D. SYSTEM PERFORMANCE

To measure the performance of ASIC and MEMS together, for all following measurements sensor element 9.4 is connected to channel 1 of the current reuse amplifier, sensor element 9.1 to channel 2 and sensor element 9.2 to channel 3. The whole measurement setup is shown in Fig. 11. Noise and signal measurements were conducted to test the whole sensor system in regard to operation as single sensors and as an array. The demodulated amplitude spectra are shown in Fig. 12 and a summary of the key parameters is given in Table 1. For the individual channels, the noise floor e is the average of the amplitude density spectrum in the vicinity of $f = 10$ Hz. The overall system noise settles around 4 μV/$\sqrt{}$Hz. Across all channels the applied alternating magnetic field modulates the excitation voltage in amplitude. It can be retrieved in the amplitude spectrum as a side peak next to the excitation frequency and yields a signal of

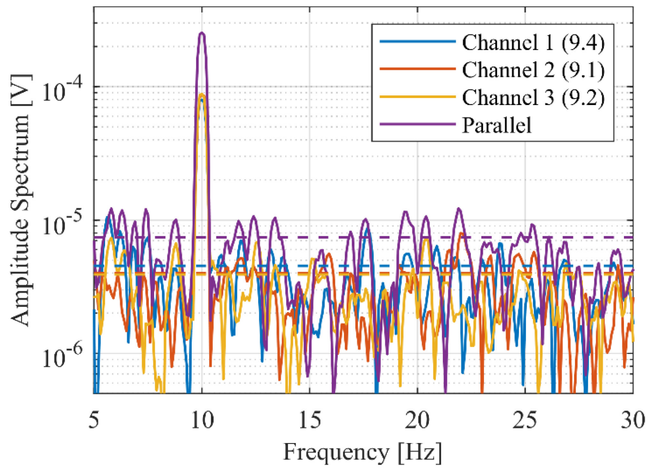

FIGURE 12. Amplitude spectra of the signals for all sensor channels after demodulation into the baseband and the calculation of a parallel readout signal. The dashed lines show the calculated noise floor.

$v_{peak} = 80$ μV to 88 μV in the spectrum. The amplitude modulation sensitivity

$$S_{AM} = \frac{v_{peak}\sqrt{2}}{B_{AC}} \tag{6}$$

can be calculated as 225 V/T to 249 V/T. The LOD is given by

$$LOD_{AM} = \frac{e}{S_{AM}} \tag{7}$$

and yields 16 nT/$\sqrt{}$Hz to 20 nT/$\sqrt{}$Hz per channel.

For the calculation of the three channels in parallel, the demodulated time domain data is further processed in MATLAB software. To synchronize the data, a cross-correlation is used to determine timing offset between datasets. Afterwards, the datasets are shifted to a matching position and added up in the time domain. Then the amplitude and amplitude density spectra are calculated and the same quantities as for the single measurements are derived. The results are compared in Fig. 12 and Table 1 respectively. Sensitivity is increased to 718 V/T, noise reduced to 7.4 μV/$\sqrt{}$Hz and the LOD is decreasing to 10 nT/$\sqrt{}$Hz. A slight discrepancy compared to adding the sensitivity values directly is observed, mainly because of rounding effects and imperfect synchronization of the time data.

IV. DISCUSSION

The current-reuse amplifier presented here offers a NEF of about 2.7 with the measured current consumption of 66 μA per channel and an IRN of 8 nV/$\sqrt{}$Hz. Overall channel 1 with sensor element 9.4 performs slightly worse compared to channel 2 and 3 with sensor element 9.1 respective 9.2 regarding noise and gain. Since the amplifiers channels behave very similar, this difference is attributed to varying sensitivity of the magnetostrictive layers deposited on the sensor elements. Here, sensor element 9.4 offers lower

TABLE 1. Measured quantities of the sensor system with $F_r = 343.6$ kHz, $v_{ex} = 0.1$ V, $B_{AC} = 500$ nT and $F_{AC} = 10$ Hz.

Amplifier channel (Sensor)	Amplitude at 10 Hz [μV]	Sensitivity [V/T]	Noise density [μV/√Hz]	LOD [nT/√Hz]
Channel 1 (9.4)	79.7	225.4	4.53	20.1
Channel 2 (9.1)	86.9	245.9	3.99	16.2
Channel 3 (9.2)	88.2	249.6	3.90	15.6
All Channels Parallel	254.1	718.6	7.43	10.3

sensitivity in comparison to the other two. This could also be confirmed in additional measurements with the same setup as used in [32].

In Table 2 a comparison to a selection of other amplifiers for biomedical applications is given. The IRN of the presented amplifier is close to [36] and [43] especially considered the small bandwidth of the other reported circuits. The noise floor is comparable to [29]. The NEF of all reported amplifiers is very close ranging from 2.2 to 3.2. For multi-channel systems an area comparison is important. Since the area is heavily dependent on the used technology node size here, as a figure of merit a normalized area is calculated, dividing the area/channel by the square of the node size [33]. The presented amplifier in this paper uses the smallest normalized area.

The sensor system exhibits a sensitivity around 250 V/T and a LOD of 16 nT/$\sqrt{}$Hz for single channels when the resonators are excited in the resonance mode at 343 kHz. The sensor resonance frequencies match well, yielding the expected signal improvement when all channels are added. The sensor elements also have similar properties regarding their noise and sensitivity, and the amplifier exhibits highly similar behavior on its three channels to enable parallel recording of three channels as shown in Fig. 12. Adding the parallel sensor channels offers increased sensitivity by a factor of 3.18, 2.92 or 2.87 in comparison to the single channel 1, 2 or 3 respectively. The amplifier operates in open-loop configuration and thus die-to-die gain variation and temperature effects are expected. Still, the measured results confirm that on-die matching of amplifier channels is sufficient for the parallel usage of three channels: The presented setup increases the signal amplitude almost by the theoretically achievable factor of 3, while the noise increases roughly with the expected factor of $\sqrt{3}$. This results in an improvement of the LOD by a factor of 1.95, 1.57 and 1.51 respectively. For the sensitivity and the LOD the performance of channel 1 increases more than the theory suggests. This is due to the better performance of the other channels. The presented approach can principally be scaled to more than three channels to further improve the LOD.

TABLE 2. Comparison of this work to other published biomedical amplifiers.

	This work	JTCASIIEB '21 [29]	JSSC '13 [36]	SVLSIC '18 [43]
Technology [nm]	350	180	130	180
Input transistors	L-BJT	L-BJT	CMOS	CMOS
Supply voltage [V]	3	3.3	1.5	1.2
Bandwidth [Hz]	100 – 75 k	0.1 - 39.2 k	19.9 k	8 k
Gain [dB]	40	40	40	60
IRN [μVrms]	3.9	-	3.7	3.4
Noise floor [nV/√Hz]	8	5.53	-	24.5
NEF	2.7	3.22	3	2.2
Power/ch. [μW]	199	481.8	13.4	5.5
Area/ch. [mm^2]	0.0288	0.297	0.03125	0.073
Normalized area/ch.	235 k	9.2 M	1.8 M	2.2 M

V. CONCLUSION

In this work it was shown that the MEMS and ASIC designs are suitable for a complete multi-channel recording system. The MEMS production process yields almost identical sensor elements capable of parallel usage to improve sensitivity and LOD. The setup shows, that this approach is scalable to bigger numbers without principle difficulties. In the future, exchange bias layers [23], [32] could be implemented, to generate the needed B_{DC} bias field directly on the sensor elements, making the external coil unnecessary. To further improve the sensitivity and reduce the noise of the resonators, findings from [44] can be implemented in the measurement process, especially regarding the optimal excitation amplitude. The presented system is very compact with microscopic MEMS sensors and a densely stacked multi-channel amplifier, all while offering low-noise low-power performance.

REFERENCES

[1] C. P. O. Treutler, "Magnetic sensors for automotive applications," *Sens. Actuators A, Phys.*, vol. 91, no. 1, pp. 2–6, Jun. 2001, doi: 10.1016/S0924-4247(01)00621-5.

[2] C. Bald and G. Schmidt, "Processing chain for localization of magnetoelectric sensors in real time," *Sensors*, vol. 21, no. 16, p. 16, Jan. 2021, doi: 10.3390/s21165675.

[3] L. Panina and M. Nemirovich, "Magnetic sensors for diagnosis and healthcare applications," in *Magnetic Sensors and Actuators in Medicine* (Woodhead Publishing Series in Electronic and Optical Materials), H. Chiriac and N. Lupu, Eds., Sawston, U.K.: Woodhead Publ., 2023, pp. 5–25, doi: 10.1016/B978-0-12-823294-1.00008-7.

[4] A. Singh, D. Mitra, B. Mandal, P. Basuchowdhuri, and R. Augustine, "A review of electromagnetic sensing for healthcare applications," *AEU Int. J. Electron. Commun.*, vol. 171, Nov. 2023, Art. no. 154873, doi: 10.1016/j.aeue.2023.154873.

[5] G. Lin, D. Makarov, and O. G. Schmidt, "Magnetic sensing platform technologies for biomedical applications," *Lab Chip*, vol. 17, no. 11, pp. 1884–1912, May 2017, doi: 10.1039/C7LC00026J.

[6] K. Gao, "Architecture for hard disk drives," *IEEE Magn. Lett.*, vol. 9, pp. 1–5, 2018, doi: 10.1109/LMAG.2018.2789888.

[7] M. Díaz-Michelena, "Small magnetic sensors for space applications," *Sensors*, vol. 9, no. 4, pp. 2271–2288, Apr. 2009, doi: 10.3390/s90402271.

[8] C. Dong et al., "Thin film magnetoelectric sensors toward biomagnetism: Materials, devices, and applications," *Adv. Electron. Mater.*, vol. 8, no. 6, 2022, Art. no. 2200013, doi: 10.1002/aelm.202200013.

[9] M. Bichurin et al., "Magnetoelectric magnetic field sensors: A review," *Sensors*, vol. 21, no. 18, p. 6232, Jan. 2021, doi: 10.3390/s21186232.

[10] Y. Wang, J. Li, and D. Viehland, "Magnetoelectrics for magnetic sensor applications: status, challenges and perspectives," *Mater. Today*, vol. 17, no. 6, pp. 269–275, Jul. 2014, doi: 10.1016/j.mattod.2014.05.004.

[11] Y. Shen, J. Gao, Y. Wang, J. Li, and D. Viehland, "Thermal stability of magnetoelectric sensors," *Appl. Phys. Lett.*, vol. 100, no. 17, Apr. 2012, Art. no. 173505, doi: 10.1063/1.4705298.

[12] A. Kumar, J. A. Chelvane, and A. Arockiarajan, "Thermally stable multi-directional magnetoelectric based embedded magnetic sensor," *Smart Mater. Struct.*, vol. 32, no. 4, Mar. 2023, Art. no. 45012, doi: 10.1088/1361-665X/acbf8e.

[13] Z. Zhang et al., "Enhancing delta E effect at high temperatures of galfenol/Ti/single-crystal diamond resonators for magnetic sensing," *ACS Appl. Mater. Interfaces*, vol. 12, no. 20, pp. 23155–23164, May 2020, doi: 10.1021/acsami.0c06593.

[14] Z. Zhang et al., "On-chip diamond MEMS magnetic sensing through multifunctionalized magnetostrictive thin film," *Adv. Funct. Mater.*, vol. 33, no. 27, 2023, Art. no. 2300805, doi: 10.1002/adfm.202300805.

[15] E. Yarar et al., "Inverse bilayer magnetoelectric thin film sensor," *Appl. Phys. Lett.*, vol. 109, no. 2, Jul. 2016, Art. no. 22901, doi: 10.1063/1.4958728.

[16] S. Zuo et al., "Ultrasensitive magnetoelectric sensing system for pico-Tesla magnetomyography," *IEEE Trans. Biomed. Circuits Syst.*, vol. 14, no. 5, pp. 971–984, Oct. 2020, doi: 10.1109/TBCAS.2020.2998290.

[17] J. Reermann et al., "Evaluation of magnetoelectric sensor systems for cardiological applications," *Measurement*, vol. 116, pp. 230–238, Feb. 2018, doi: 10.1016/j.measurement.2017.09.047.

[18] J. Reermann, S. Zabel, C. Kirchhof, E. Quandt, F. Faupel, and G. Schmidt, "Adaptive readout schemes for thin-film magnetoelectric sensors based on the delta-E effect," *IEEE Sensors J.*, vol. 16, no. 12, pp. 4891–4900, Jun. 2016, doi: 10.1109/JSEN.2016.2553962.

[19] N. Akulov and E. Kondorsky, "Über einen magnetomechanischen Effekt," *Zeitschrift für Physik*, vol. 78, no. 11, pp. 801–807, Nov. 1932, doi: 10.1007/BF01342040.

[20] R. Kimura, "On the elastic moduli of ferromagnetic materials. Part II. The change in young's modulus, due to magnetisation and temperature," *Proc. Physico-Math. Soc. Jpn. 3rd Ser.*, vol. 21, no. 12, pp. 786–799, 1939, doi: 10.11429/ppmsj1919.21.12_786.

[21] B. Spetzler, C. Kirchhof, E. Quandt, J. McCord, and F. Faupel, "Magnetic sensitivity of bending-mode delta-E-effect sensors," *Phys. Rev. Appl.*, vol. 12, no. 6, Dec. 2019, Art. no. 64036, doi: 10.1103/PhysRevApplied.12.064036.

[22] S. Zabel et al., "Multimode delta-E effect magnetic field sensors with adapted electrodes," *Appl. Phys. Lett.*, vol. 108, no. 22, May 2016, Art. no. 222401, doi: 10.1063/1.4952735.

[23] B. Spetzler et al., "Exchange biased delta-E effect enables the detection of low frequency pT magnetic fields with simultaneous localization," *Sci. Rep.*, vol. 11, no. 1, p. 5269, Dec. 2021, doi: 10.1038/s41598-021-84415-2.

[24] T. Nan, Y. Hui, M. Rinaldi, and N. X. Sun, "Self-biased 215MHz magnetoelectric NEMS resonator for ultra-sensitive DC magnetic field detection," *Sci. Rep.*, vol. 3, no. 1, p. 1985, Jun. 2013, doi: 10.1038/srep01985.

[25] A. D. Matyushov et al., "Curvature and stress effects on the performance of contour-mode resonant ΔE effect magnetometers," *Adv. Mater. Technol.*, vol. 6, no. 9, 2021, Art. no. 2100294, doi: 10.1002/admt.202100294.

[26] V. Schell et al., "Exchange biased surface acoustic wave magnetic field sensors," *Sci Rep*, vol. 13, no. 1, p. 8446, May 2023, doi: 10.1038/s41598-023-35525-6.

[27] A. Kittmann et al., "Wide band low noise love wave magnetic field sensor system," *Sci. Rep.*, vol. 8, no. 1, p. 278, Dec. 2018, doi: 10.1038/s41598-017-18441-4.

[28] J. Schmalz et al., "Multi-mode love-wave SAW magnetic-field sensors," *Sensors*, vol. 20, no. 12, p. 3421, Jan. 2020, doi: 10.3390/s20123421.

[29] H. Kim et al., "Low-noise chopper amplifier using lateral PNP input stage with automatic base current cancellation," *IEEE Trans. Circuits Syst. II, Exp. Briefs*, vol. 68, no. 7, pp. 2297–2301, Jul. 2021, doi: 10.1109/TCSII.2021.3063358.

[30] D. Zhao, M. F. Zaman, and F. Ayazi, "A chopper-stabilized lateral-BJT-input interface in 0.6μm CMOS for capacitive accelerometers," in *IEEE Int. Solid-State Circuits Conf. Tech. Dig.*, Feb. 2008, pp. 584–637. doi: 10.1109/ISSCC.2008.4523318.

[31] E. A. Vittoz, "MOS transistors operated in the lateral bipolar mode and their application in CMOS technology," *IEEE J. Solid-State Circuits*, vol. 18, no. 3, pp. 273–279, Jun. 1983, doi: 10.1109/JSSC.1983.1051939.

[32] B. Spetzler et al., "Modeling and parallel operation of exchange-biased delta-E effect magnetometers for sensor arrays," *Sensors*, vol. 21, no. 22, p. 7594, Jan. 2021, doi: 10.3390/s21227594.

[33] S. Simmich, P. Wiegand, and R. Rieger, "Noise efficient three-channel amplifier for MEMS cantilever readout," in *Proc. IEEE Asia Pac. Conf. Circuits Syst. (APCCAS)*, Nov. 2023, pp. 164–168. doi: 10.1109/APCCAS60141.2023.00046.

[34] F. Ilgaz et al., "Miniaturized double-wing ΔE-effect magnetic field sensors," *Sci. Rep.*, vol. 14, no. 1, May 2024, Art. no. 11075, doi: 10.1038/s41598-024-59015-5.

[35] C. D. Motchenbacher and F. C. Fitchen, *Low-Noise Electronic Design*. Hoboken, NJ, USA: Wiley, 1973.

[36] B. Johnson and A. Molnar, "An orthogonal current-reuse amplifier for multi-channel sensing," *IEEE J. Solid-State Circuits*, vol. 48, no. 6, pp. 1487–1496, Jun. 2013, doi: 10.1109/JSSC.2013.2257478.

[37] M. S. J. Steyaert and W. M. C. Sansen, "A micropower low-noise monolithic instrumentation amplifier for medical purposes," *IEEE J. Solid-State Circuits*, vol. 22, no. 6, pp. 1163–1168, Dec. 1987, doi: 10.1109/JSSC.1987.1052869.

[38] M. Rezaei, E. Maghsoudloo, C. Bories, Y. De Koninck, and B. Gosselin, "A low-power current-reuse analog front-end for high-density neural recording implants," *IEEE Trans. Biomed. Circuits Syst.*, vol. 12, no. 2, pp. 271–280, Apr. 2018, doi: 10.1109/TBCAS.2018.2805278.

[39] R. Jahns, R. Knöchel, H. Greve, E. Woltermann, E. Lage, and E. Quandt, "Magnetoelectric sensors for biomagnetic measurements," in *Proc. IEEE Int. Symp. Med. Meas. Appl.*, May 2011, pp. 107–110. doi: 10.1109/MeMeA.2011.5966676.

[40] P. Durdaut, V. Penner, C. Kirchhof, E. Quandt, R. Knochel, and M. Hoft, "Noise of a JFET charge amplifier for piezoelectric sensors," *IEEE Sensors J.*, vol. 17, no. 22, pp. 7364–7371, Nov. 2017, doi: 10.1109/JSEN.2017.2759000.

[41] P. Durdaut et al., "Modeling and analysis of noise sources for thin-film magnetoelectric sensors based on the delta-E effect,"'*IEEE Trans. Instrum. Meas.*, vol. 66, no. 10, pp. 2771–2779, Oct. 2017, doi: 10.1109/TIM.2017.2709478.

[42] H. Jin, S. R. Dong, J. K. Luo, and W. I. Milne, "Generalised Butterworth-Van Dyke equivalent circuit for thin-film bulk acoustic resonator," *Electron. Lett.*, vol. 47, no. 7, pp. 424–426, Mar. 2011, doi: 10.1049/el.2011.0343.

[43] T. Jang et al., "A 2.2 NEF neural-recording amplifier using discrete-time parametric amplification," in *Proc. IEEE Symp. VLSI Circuits*, Jun. 2018, pp. 237–238. doi: 10.1109/VLSIC.2018.8502432.

[44] E. Spetzler, B. Spetzler, and J. McCord, "A magnetoelastic twist on magnetic noise: The connection with intrinsic nonlinearities," *Adv. Funct. Mater.*, vol. 34, no. 9, 2024, Art. no. 2309867, doi: 10.1002/adfm.202309867.

PATRICK WIEGAND received the M.Sc. degree in electrical and information engineering from Kiel University, Germany, in 2018, where he is currently pursuing the Ph.D. degree with the Chair for Networked Electronic Systems, Department of Electrical and Information Engineering. His research interests include thin-film magnetoelectric sensors and sensor interfaces on ASICs.

SEBASTIAN SIMMICH (Graduate Student Member, IEEE) received the B.Sc. and M.Sc. degrees in electrical engineering and information technology from the Christian-Albrechts-University of Kiel, Germany, in 2017 and 2018, respectively, where he is currently pursuing the Ph.D. degree with the Chair of Networked Electronic Systems, Department of Electrical Engineering and Information Technology. His research interests focus on developing low-noise and low-power CMOS circuits for biomedical applications.

FATIH ILGAZ received the M.Sc. degree in advanced materials from Ulm University, Germany, in 2020. He is currently pursuing the Ph.D. degree with the Chair for Multicomponent Materials, Department of Materials Science, Kiel University, Germany. His research interests include thin-film magnetoelectric sensors and magnetic materials.

FRANZ FAUPEL received the Ph.D. degree in physics from the University of Göttingen in 1985 and the Habilitation degree in 1992. He was a Postdoctoral Fellow with the IBM Research Center Yorktown Heights. Since 1994, he has been holding the Chair for Multicomponent Materials, Kiel University. He published more than 400 research papers on metallic glasses, metal-polymer interfaces, functional nanocomposites, magnetoelectric sensors, photocatalysis, plasma deposition, and memristive devices for neuromorphic computing. He is the Chairman of the North European Initiative Nanotechnology and a Founding Member of the newly established International Alliance of Societies for a Sustainable Future. He has served on various editorial boards, including the *Journal of Materials Research*, *SN Applied Sciences*, *Materials*, *Applied Physics Letters*, and *Journal of Applied Physics*. For more information, see www.tf.uni-kiel.de/matwis/matv.

BENJAMIN SPETZLER (Member, IEEE) received the M.Sc. and Ph.D. degrees in materials science and engineering from the University of Kiel, Kiel, Germany, in 2017, and 2021, respectively. Since then, he has been a Postdoctoral Researcher and a Group Leader within the Chair of Micro- and Nanoelectronic Systems, TU Ilmenau, Ilmenau, Germany. His research interests include magnetic field sensing with magnetoelectric composites as well as the modeling of electronic materials and systems for neuromorphic computing.

ROBERT RIEGER (Senior Member, IEEE) received the B.Eng. degree from the University of Kent, Canterbury, U.K., in 2000, and the Ph.D. degree in electrical and electronics engineering from University College London, London, U.K., in 2004. From 2004 to 2005, he was a Design Engineer with austriamicrosystems AG, Switzerland. He joined the Electrical Engineering Department, National Sun Yat-Sen University, Kaohsiung, Taiwan, where he headed the Bionics Integrated Systems Laboratory from 2006 to 2018. Since 2018, he has been a Professor with Kiel University, Germany, where he holds the Chair of Networked Electronic Systems. His research interests are in the area of low-power electronics for biomedical application and bio-sensing and processing electronics design. He has served on various editorial boards, including as the 2022–2023 Digital Communications Associate Editor-in-Chief for IEEE TRANSACTIONS ON BIOMEDICAL CIRCUITS AND SYSTEMS and as an Associate Editor for the IEEE TRANSACTIONS ON CIRCUITS AND SYSTEMS–I: REGULAR PAPERS. He is the Founding Officer and the Past Chairman of the IEEE Engineering in Medicine and Biology Society Tainan Chapter. He is also a member of the IEEE Technical Committees on Biomedical and Life Science Circuits and Systems, VLSI Systems and Applications, and Circuits and Systems Education and Outreach.